IOP Publishing and International Atomic Energy Agency Nuclear Fusion
Nucl. Fusion **53** (2013) 093006 (8pp) doi:10.1088/0029-5515/53/9/093006

The effect of the fast-ion profile on Alfvén eigenmode stability

W.W. Heidbrink[1], M.A. Van Zeeland[2], M.E. Austin[3], E.M. Bass[4], K. Ghantous[5], N.N. Gorelenkov[5], B.A. Grierson[5], D.A. Spong[6] and B.J. Tobias[5]

[1] University of California Irvine, Irvine, CA, USA
[2] General Atomics, San Diego, CA, USA
[3] University of Texas at Austin, Austin, TX, USA
[4] University of California San Diego, San Diego, CA, USA
[5] Princeton Plasma Physics Laboratory, Princeton, NJ, USA
[6] Oak Ridge National Laboratory, Oak Ridge, TN, USA

Received 9 April 2013, accepted for publication 22 July 2013
Published 9 August 2013
Online at stacks.iop.org/NF/53/093006

Abstract
Different combinations of on-axis and off-axis neutral beams are injected into DIII-D plasmas that are unstable to reversed shear Alfvén eigenmodes (RSAE) and toroidal Alfvén eigenmodes (TAE). The variations alter the classically expected fast-ion gradient $\nabla\beta_f$ in the plasma interior. Off-axis injection reduces the amplitude of RSAE activity an order of magnitude. Core TAEs are also strongly stabilized. In contrast, at larger minor radius, the fast-ion gradient is similar for on- and off-axis injection and switching the angle of injection has a weaker effect on the stability of TAEs. The average mode amplitude correlates strongly with the classically expected profile but the measured profile relaxes to similar values independent of the fraction of off-axis beams. The observations agree qualitatively with a 'critical-gradient' model of fast-ion transport.

(Some figures may appear in colour only in the online journal)

1. Introduction

Toroidal Alfvén eigenmodes (TAEs) [1–3] and reversed shear Alfvén eigenmodes (RSAE—also called 'Alfvén cascades') [4–6] are instabilities that are driven unstable by energetic ion populations in toroidal plasmas. They are potentially unstable in future burning plasmas such as ITER [7]. Competition between the fast-ion drive and damping on the background plasma determines mode stability. In principle, the modes could be driven by velocity-space gradients but, in practice, configuration-space gradients usually drive the instabilities. In a classic early theory paper [8], the fast-ion drive γ/ω is proportional to the gradient of the fast-ion beta, $\nabla\beta_f$.

Experimentally, the leading technique for measurement of damping rates uses an antenna to measure the Q-factor of stable modes [9]. To study fast-ion drive, experimenters usually vary the heating power to find the marginal stability point. (See [10] for an early example.) A complication in such studies is that, in addition to changing the fast-ion gradient, variations in heating power also alter the background plasma parameters, so the damping rate is also affected. To minimize this effect, in this paper, the fast-ion gradient is changed *at nearly constant heating power.*

The gradient is changed by injecting different combinations of on-axis and off-axis beams. The DIII-D tokamak is equipped with eight neutral-beam sources housed in four beamlines. A hydraulic lift can elevate one of the beamlines to steer the beam vertically [11]. When the beamline is elevated, the pair of sources in this beamline aim through a midplane port to a point below the centre in the plasma. For the elevation utilized in this study, the off-axis beams deposit large numbers of ions near $\rho \simeq 0.5$, where ρ is the normalized square root of the toroidal flux. Initial experiments with the elevated sources confirm that, in MHD-quiescent plasmas, the off-axis sources can produce hollow fast-ion profiles [12].

The idea of the present experiment is to inject off-axis beams during the current ramp into a plasma that would have strong TAE and RSAE instabilities with on-axis injection. This plasma condition is selected for three reasons. First, the threshold for instability with on-axis injection is quite low (~1 MW), so the available off-axis power (~4 MW) is more than adequate. Second, this condition has been thoroughly studied in the past, so the properties are well understood. The discharges are similar to earlier discharges with radial eigenfunctions that resemble the radial eigenfunctions calculated by ideal MHD [13–15] with the exception that radial shearing of the mode phase [16, 17] is observed. The linear stability of the eigenmodes has been studied by gyrofluid [18] and gyrokinetic [18, 19] codes.

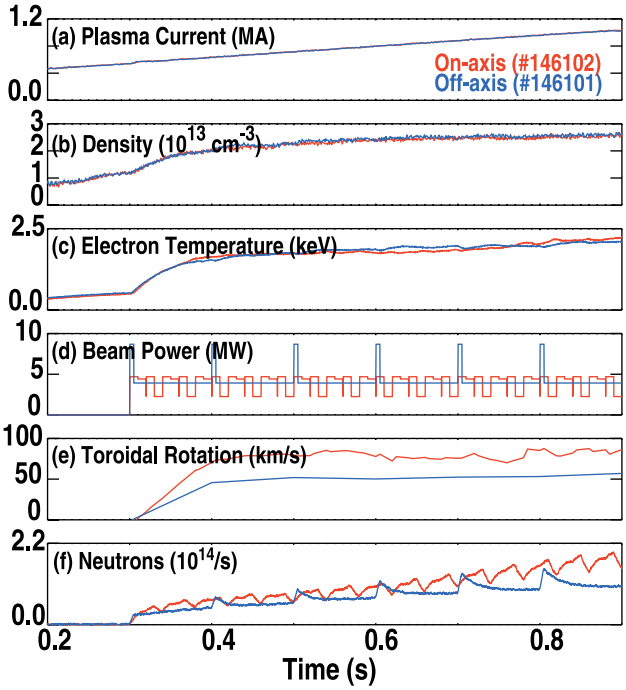

Figure 1. Time evolution of (*a*) plasma current I_p, (*b*) line-average electron density $\bar{n}_e$, (*c*) central electron temperature T_e, (*d*) reported beam power, (*e*) central toroidal rotation and (*f*) neutron rate in a pair of similar discharges with either on-axis or off-axis injection. In the off-axis case, short 10 ms pulses of on-axis beams are injected every 100 ms for diagnostics. Toroidal field $B_T = -2.0$ T.

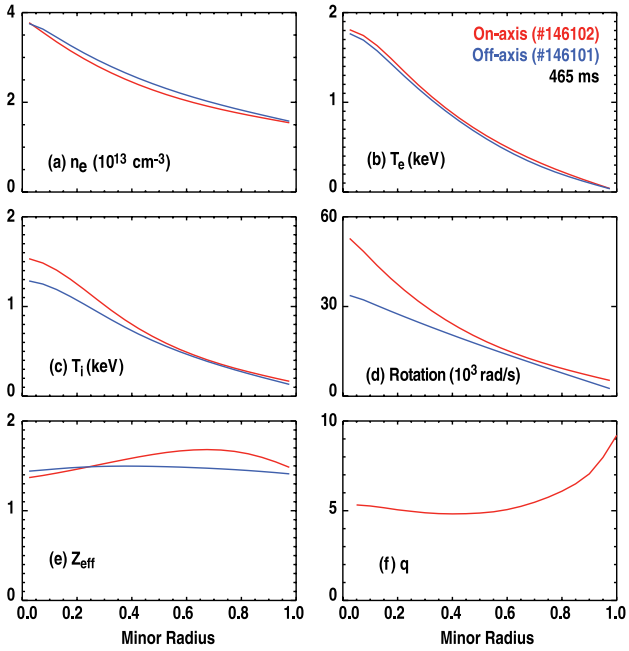

Figure 2. Profiles at 465 ms of (*a*) electron density, (*b*) electron temperature, (*c*) ion temperature, (*d*) toroidal angular velocity, (*e*) Z_{eff} and (*f*) safety factor versus normalized minor radius ρ for the same pair of discharges shown in figure 1.

During on-axis injection, these operating conditions lead to strong flattening of the fast-ion profile [20, 21] and to beam-ion losses [22]. Many of these phenomena have been reproduced in ASDEX-Upgrade [23]. A third advantage of this condition is the mode saturation mechanism, which is likely to be relevant to future devices like ITER. Because there are many small amplitude resonances, the fast-ion transport is governed by stochastic overlap of many modes [24, 25] and the final profile resembles the one computed by quasilinear theory [26].

The paper begins with a description of the experimental conditions (section 2). Section 3 contains the main results: the amplitude of RSAE and TAE activity depends strongly on the calculated fast-ion gradient. Section 4 compares the data with linear stability calculations and with predicted fast-ion profiles. The conclusions are in section 5.

2. Experimental conditions

The plasma shape is either an oval (elongation $\kappa \simeq 1.6$, triangularity $\delta < 0.1$) or a nearly circular plasma ($\kappa \simeq 1.2$, $\delta < 0.1$) that is limited on the inside wall. The plasma is deuterium, the neutral beams inject deuterium atoms, and the primary impurity is carbon from the graphite walls ($Z_{eff} \simeq 1.5$). The neutral beams inject during the current ramp (figure 1(*a*)). The density (figure 1(*b*)) is relatively low ($\sim 2.5 \times 10^{13}$ cm^{-3}) and the plasma remains in L-mode. The density and electron temperature (figure 1(*c*)) are well matched on discharges with different combinations of on-axis and off-axis injection. The energetic ion population is produced by deuterium neutral-beam injection of 75–81 keV neutrals. Co-injection in the direction of the plasma current is employed.

Since the different sources inject different amounts of beam power, the duty cycle of the injected sources is adjusted so that the average power is similar for on-axis and off-axis injection (figure 1(*d*)). The optics for the motional Stark effect (MSE) [27], charge-exchange recombination (CER) [28], and fast-ion D-alpha (FIDA) [29–31] diagnostics view on-axis sources so, to diagnose the off-axis cases, brief pulses of diagnostic beams are injected at 10% duty cycle (or less) in the off-axis discharges. On-axis injection produces larger central toroidal rotation than off-axis injection (figure 1(*e*)). The neutron rate (figure 1(*f*)) is also somewhat higher for on-axis injection but, in both cases, the rate is below the classical prediction during the time of interest.

Figure 2 shows a comparison of plasma profiles at a time of interest. The electron density and temperature and Z_{eff} are well matched in comparisons between on-axis and off-axis injection but the central ion temperature and toroidal rotation are higher during on-axis injection.

The q profile (figure 2(*f*)) is reversed with the minimum value at a minor radius near 0.45. Because the MSE diagnostic utilizes an on-axis beam, only sparse q profile measurements are available during off-axis injection. The available data indicate that the q profiles are very similar at the time of interest in comparison discharges, presumably because neutral-beam current drive has little effect on current diffusion early in the discharge. Nevertheless, because the q profile plays such an important role in Alfvén eigenmode stability, the evolution of the profile was altered by changing the starting time of neutral-beam injection from 300 to 250 ms, without a noticeable effect on the stability results reported here.

The goal of the experiment is to study the effect of the spatial gradient $\nabla\beta_f$ on AE stability. To minimize changes in velocity space, in comparisons between on-axis and

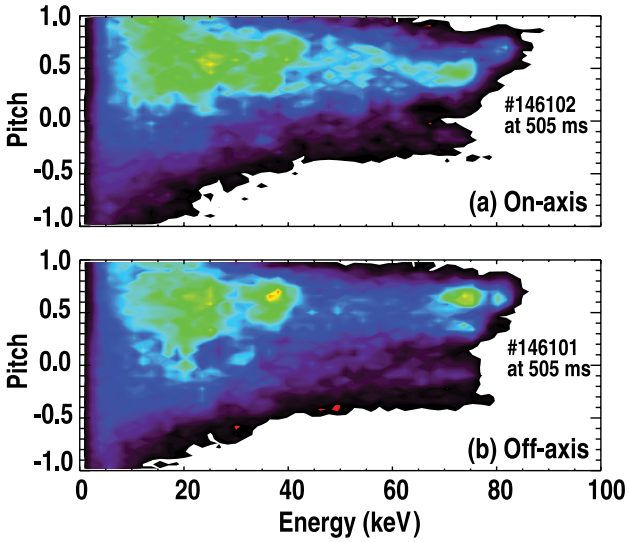

Figure 3. NUBEAM calculation of the fast-ion distribution function at 505 ms for the same pair of discharges shown in figure 1. The distribution is averaged over a spatial region that is near $q_{\min}$ on the outside ($R > R_0$) of the plasma. The calculations use the reported beam power.

off-axis injection, equal numbers of near-tangential (tangency radius $R_{\tan} \simeq 115$ cm) and near-perpendicular ($R_{\tan} \simeq 76$ cm) sources are used. The TRANSP NUBEAM code [32] predicts the fast-ion distribution in the absence of transport by instabilities. Comparison of on-axis and off-axis cases shows that the velocity-space distributions are indeed similar (figure 3).

The toroidal field is $B_T \simeq 2.0$ T but both clockwise and counter-clockwise directions are employed. For off-axis injection, the helicity of the magnetic field alters the fraction of trapped particles [12, 33]. The favourable helicity for neutral-beam current drive (called $+B_T$ here) has more passing particles and more off-axis fast ions than the unfavourable ($-B_T$) helicity.

The experiments matched beam powers for different conditions using the beam powers reported by the DIII-D neutral-beam group. Subsequent experiments in MHD-quiescent plasmas [12] found discrepancies between the measured and calculated neutron rates that imply errors in the reported beam powers. In this paper, we distinguish between the 'reported beam power' and the 'corrected beam power' that is calculated using factors inferred from these special discharges.

3. Experimental results

Figure 4 illustrates the idea of the experiment. Since the off-axis beam deposition peaks near $\rho = 0.5$, variation between on-axis and off-axis injection has a large effect on $\nabla\beta_f$ in the central half of the plasma but has a smaller effect for $\rho \gtrsim 0.5$. The radial eigenfunction for an RSAE is localized near $q_{\min}$, so RSAE stability should depend strongly on the injection location; similarly, core TAEs [34] with eigenfunctions that are localized inside $q_{\min}$ should be strongly affected. On the other hand, a global TAE with a radial

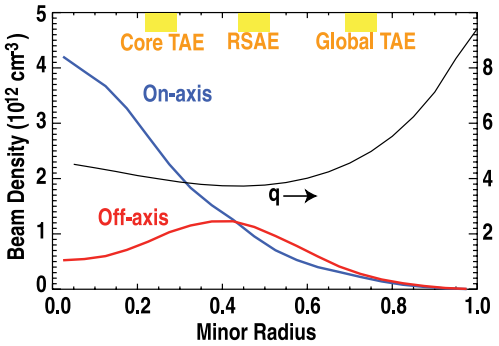

Figure 4. Concept of the experiment. Core TAEs occur inside of $q_{\min}$ where the fast-ion profile is flat or hollow with off-axis injection, RSAEs occur near $q_{\min}$ where $\nabla\beta_f$ is small during off-axis injection, and global TAEs lie in a region where the gradient is insensitive to changes between on-axis and off-axis injection. The illustrated fast-ion profiles are from classical calculations performed prior to the experiment.

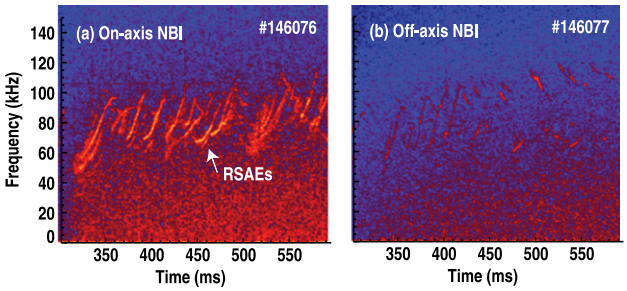

Figure 5. Cross power of adjacent ECE channels that are located near $q_{\min}$ (at $R \simeq 195$ cm) during (*a*) on-axis and (*b*) off-axis injection. The same logarithmic colour scale is used in both figures. In the off-axis case, the mode activity at 400 and 500 ms coincides with brief diagnostic blips of the on-axis beams.

eigenfunction that extends into the outer half of the plasma should depend weakly on the deposition location.

These expectations are in excellent qualitative agreement with the observations. Figure 5 compares spectrograms from a pair of electron cyclotron emission (ECE) channels that are located near $q_{\min}$. During on-axis injection, strong RSAEs are observed. As is characteristic for RSAEs [5], the frequency of each RSAE sweeps upward from approximately the geodesic acoustic mode (GAM) frequency to the TAE frequency as the q profile evolves. In contrast, for off-axis injection, hardly any modes are observed. (Most of the visible modes in figure 5(*b*) occur during on-axis diagnostic blips at 400 and 500 ms.) For this paper, the 40-channel ECE radiometer that measures a radial profile of T_e fluctuations near the midplane [35] is the primary fluctuation diagnostic. Similar results are obtained by ECE imaging [36], interferometer [37], and beam emission spectroscopy [38] diagnostics.

Outside of $q_{\min}$, TAEs are evident in the spectra (figure 6). (The TAEs are the modes with frequencies that change gradually in time.) For on-axis injection, both TAEs and relatively faint RSAEs are apparent outside $q_{\min}$ (figure 6(*a*)). For off-axis injection, outside $q_{\min}$ the TAEs are readily apparent but RSAEs are essentially absent (figure 6(*b*)). In contrast, in the core, TAEs are visible for on-axis injection (figure 6(*c*)) but absent for off-axis injection (figure 6(*d*)).

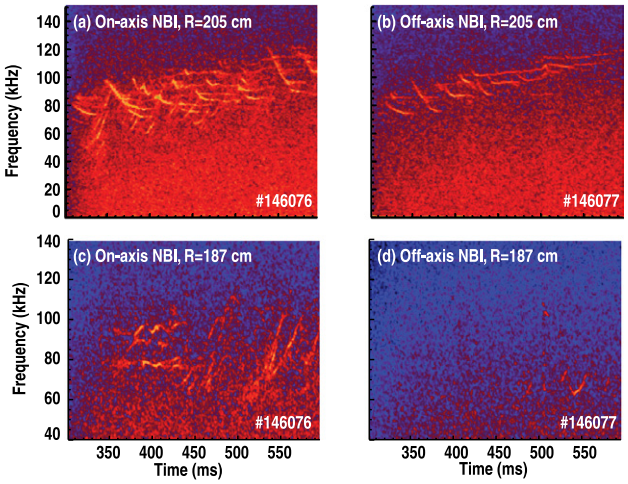

Figure 6. Cross power of adjacent ECE channels during on-axis (*a*), (*c*) and off-axis (*b*), (*d*) injection for a probe pair that is (*a*), (*b*) outside and (*c*), (*d*) inside of $q_{\min}$. The same logarithmic colour scale is used for each probe pair ((*a*) and (*b*), (*c*) and (*d*)).

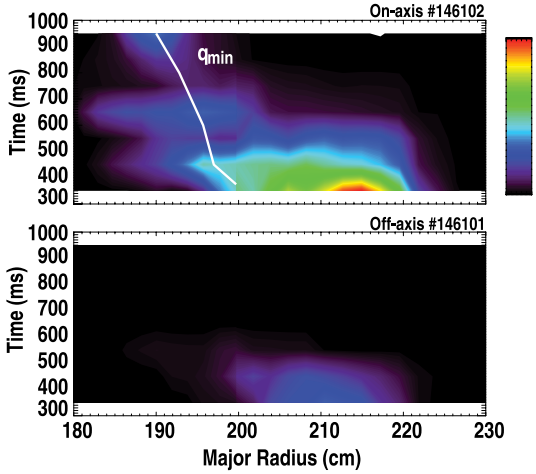

Figure 7. Summed amplitude of coherent AE activity $\sum \delta T_e/T_e$ versus major radius and time for (top) on-axis and (bottom) off-axis injection. The same rainbow colour scale is used in both contour plots. The line is the approximate location of the radius of $q_{\min}$.

To quantify these qualitative results, an automated program that identifies and measures coherent modes in the ECE data was developed. Selected modes satisfy the following criteria.

- The mode frequency lies between $0.95\,f_{GAM}$ and $1.4\,f_{TAE}$, where f_{GAM} and f_{TAE} are simple estimates of the GAM and TAE frequencies, respectively.
- The coherence between the ECE signal and two different interferometer chords must be statistically significant.
- A candidate mode must appear on at least four ECE channels.
- Modes that meet the previous criteria must persist for successive times (separated by 1.2 ms), adjacent frequencies (separated by 0.2 kHz), and adjacent spatial channels (typical separation 2 cm).

The normalized amplitude $\delta T_e/T_e$ of identified modes is stored for each ECE channel.

Figure 7 compares the output of this program for representative on-axis and off-axis cases. For both deposition profiles, the summed mode amplitude is largest early in time and outside of $q_{\min}$. For on-axis injection, modes are visible at $q_{\min}$ but are virtually absent for off-axis injection. In the core, the activity is intermittent for on-axis injection and absent for off-axis injection.

A database of mode amplitudes from the 50 discharges in the experiment was compiled. (The database avoids times close to on-axis diagnostic blips for the off-axis cases.) Figure 8 shows a controlled scan between on-axis and off-axis injection in the oval shape for a set of discharges that all had 4.0–4.5 MW of reported beam power in the $-B_T$ scan and 3.5 MW of reported power in the $+B_T$ scan. The beam mixture fraction is the ratio of off-axis to total power. A systematic variation of mode amplitude with beam mix is observed. For the favourable field helicity, mode activity is virtually absent. Irrespective of beam mix, the mode activity is weaker near the magnetic axis than it is outside of $q_{\min}$.

The trends shown in figure 8 are also observed in plasmas with nearly circular cross section (figure 9). The AEs are driven by $\nabla\beta_f$ regardless of plasma shape, so it is unsurprising that oval and circular plasmas have similar dependencies on the injected beam mix. The correlation shown in figure 8 is degraded slightly by inclusion of discharges with electron cyclotron heating.

The experimental trends shown in figures 8(*b*)–(*d*) are in excellent agreement with expectations based on the classically expected beam-ion profile. Figure 8(*a*) shows a set of NUBEAM calculations of the classically expected beam-ion density. These are the profiles that would be obtained for the measured plasma parameters if there was no anomalous fast-ion transport. To facilitate comparison, all of the calculations use identical plasma profiles; the reported neutral-beam waveforms from the shots in the beam-mix scan replace the actual beam waveform from the on-axis discharge (#146102). For the $+B_T$ case, the sign of the toroidal field is flipped within TRANSP. Comparison of the calculations with the measurements show that, as the predicted $\nabla\beta_f$ in the core becomes smaller, the amplitude of AE activity decreases.

It should be stressed that the classically predicted profiles are *not* observed in the experiment. The predictions shown in figure 8(*a*) are useful indicators of the instability drive but the true experimental profiles are flattened by the Alfvén activity, as previously reported [20, 21]. In fact, the relaxed profiles are similar for all discharges in the beam-mix scan. Figure 10(*a*) shows FIDA profiles measured with the tangentially-viewing 'main-ion CER' [31] diagnostic. Irrespective of the mixture of on-axis and off-axis beams, the fast-ion profiles are similar. The data from the other FIDA diagnostics also indicate that the fast-ion profile is nearly identical in all cases. Figure 10(*b*) compares measurements of the FIDA feature for all of the vertically-viewing FIDA channels with valid data. Within experimental uncertainties, the profiles are indistinguishable. In contrast, for both systems, at later times in these same discharges (when the Alfvén eigenmode activity weakens) substantial differences in profiles are observed.

4. Theoretical analysis

Ultimately, a complete theory of Alfvén eigenmode activity will describe the nonlinear evolution of multiple modes,

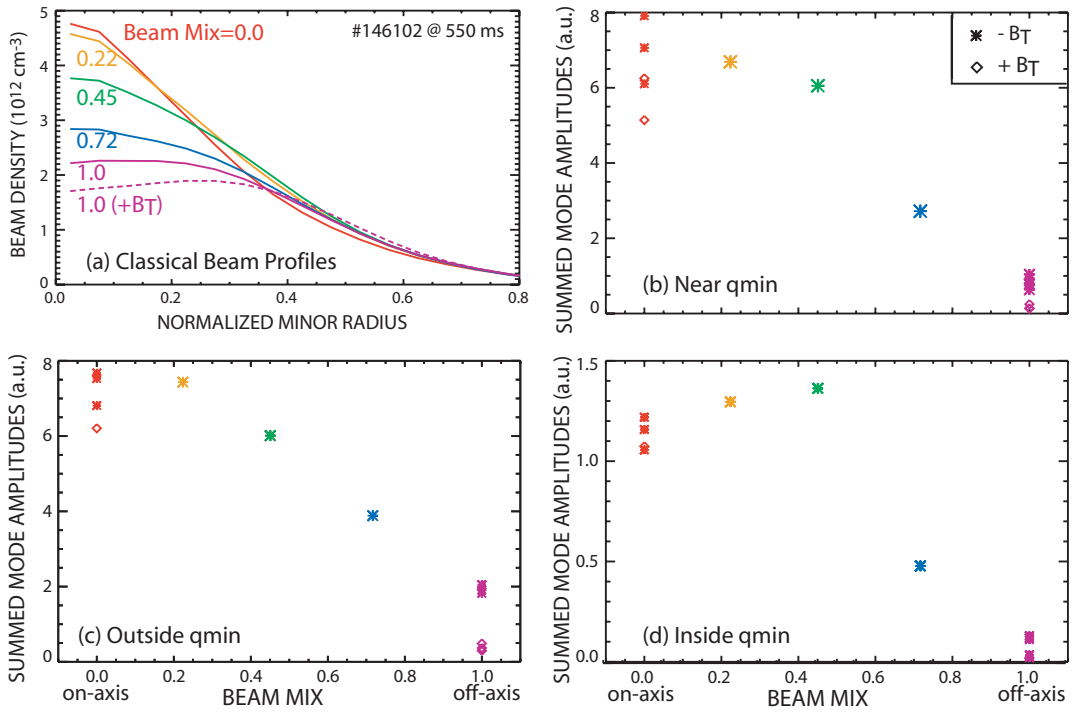

Figure 8. (*a*) NUBEAM beam density profiles versus minor radius for discharges with different combinations of on-axis and off-axis injection as calculated using the reported beam power. Summed amplitude of coherent AE activity $\sum \delta T_e/T_e$ versus the fraction of off-axis beam power for channels (*b*) near q_{min} $R \simeq 194$–202 cm, (*c*) outside q_{min} $R \simeq 204$–210 cm, and (*d*) inside q_{min} $R \simeq 186$–190 cm. The diamond symbols represent discharges with the field helicity that is favourable for neutral-beam current drive; the * symbols are the opposite helicity.

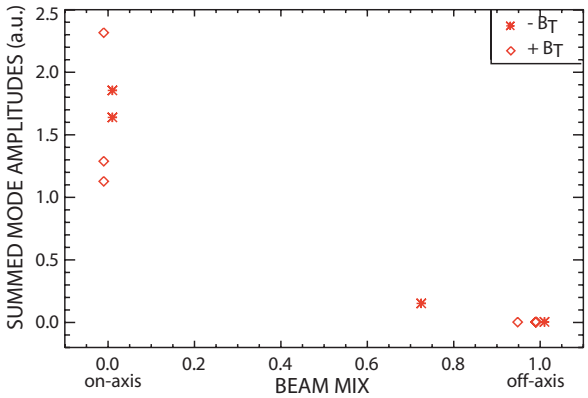

Figure 9. Summed amplitude of coherent AE activity $\sum \delta T_e/T_e$ versus the fraction of off-axis beam power for channels near q_{min} in nearly circular discharges. The diamond symbols represent discharges with the field helicity that is favourable for neutral-beam current drive; the * symbols are the opposite helicity.

including the consequent fast-ion transport; unfortunately, a full treatment is beyond present capabilities. Consequently, in this section, we utilize simpler models in pursuit of a qualitative understanding of the experimental results. Section 4.1 presents *linear* stability calculations using fast-ion profiles that would exist *in the absence of fast-ion transport*. Section 4.2 uses a 'critical-gradient' model that employs approximate linear growth rates to model fast-ion transport.

4.1. Linear stability calculations

A recent paper [18] describes a linear verification and validation exercise for the TAEFL gyro-Landau fluid code, the GTC particle-in-cell gyrokinetic code, and the GYRO continuum gyrokinetic code. The comparison case for that study is a DIII-D RSAE similar to the ones measured here. The paper reports predicted RSAE frequencies that have a magnitude and q_{min} dependence within ~10% of the measured values. The eigenmode structures predicted by the three codes resemble the measured structure but differ in detail. The growth rates predicted by the three codes are comparable in magnitude but differ from one another by as much as a factor of two.

New GYRO and TAEFL calculations of linear stability have been completed for the beam-mix scan (figure 8(*a*)). The methodology is similar to that used previously [18]. To facilitate comparison, the plasma profiles are held fixed for all six cases but the fast-ion profiles are varied using the classically predicted fast-ion profiles shown in figure 8(*a*). (The thermal ion density is adjusted to preserve quasineutrality.)

When run as an initial-value code, GYRO finds that a global TAE is the most unstable mode for all angles of beam injection. Another implementation of the GYRO code uses an eigenvalue solver that can identify subdominant modes [39]. Figure 11 shows the $n = 3$ mode structures computed by GYRO for three of the cases. The global TAE that extends beyond $\rho = 0.5$ is the most unstable mode. For on-axis injection (figure 11(*a*)), GYRO finds unstable modes in the core and near q_{min}. For the extreme off-axis case (figure 11(*c*)), the mode near q_{min} is weaker and the core modes are absent.

TAEFL is an initial-value code. Figure 12 shows the predicted mode structures of the most unstable $n = 3$ mode for the six cases. This is a mode that extends from q_{min} into the exterior of the plasma. The frequencies of these modes

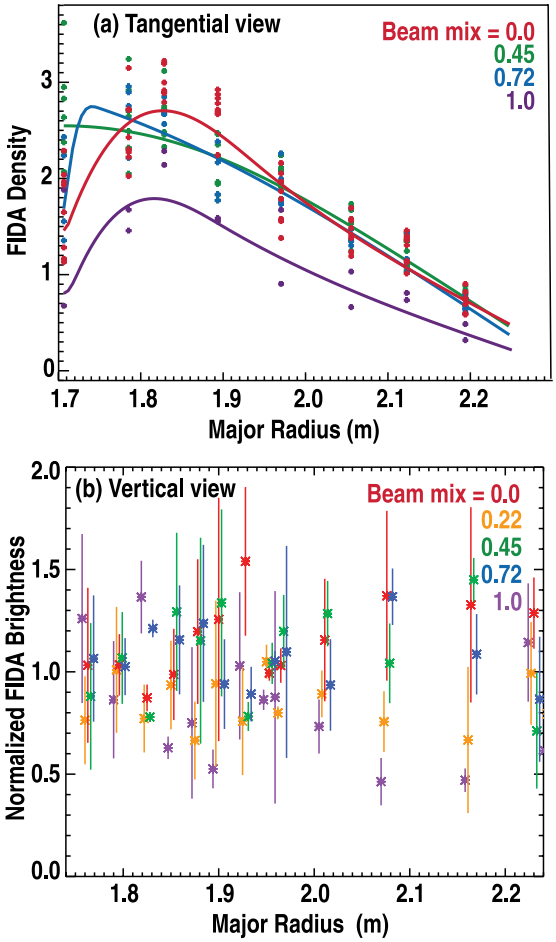

Figure 10. (*a*) FIDA data for tangentially-viewing channels. The FIDA brightness divided by the injected neutral density is plotted versus major radius for four discharges in the beam-mix scan of figure 8. The FIDA brightness is derived from a fit to the blue-shifted D_α spectrum produced by co-circulating fast ions. Each data point represents a single pulse of the active neutral beam viewed by the main-ion CER diagnostic. (*b*) FIDA data for vertically-viewing channels versus major radius for five discharges in the beam-mix scan. For each channel, the five measurements are normalized to the average value for the beam-mix scan. (The five points are displaced slightly from one another for clarity.) Wavelength integration corresponds to energies along the line-of-sight of 25–68 keV.

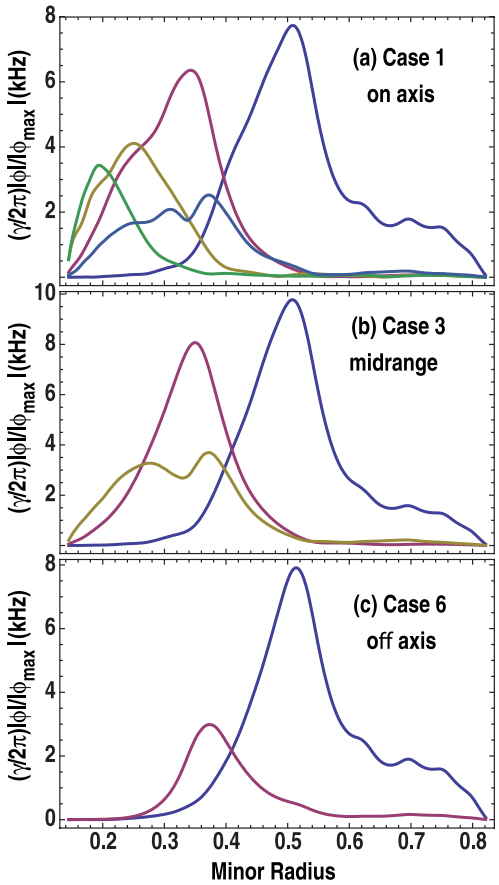

Figure 11. Midplane value of the electric potential $|\Phi|$ for the unstable $n = 3$ modes found by GYRO in three representative cases: beam mix = (*a*) 0.0, (*b*) 0.45 and (*c*) 1.0, $+B_T$. Each curve represents a different unstable eigenmode. The modes are normalized such that the highest peak is equal to the linear growth rate.

are similar in all cases, varying from 73 kHz in the plasma frame for on-axis injection to 68 kHz for off-axis injection. The mode structure becomes more global as the fast-ion profile broadens; qualitatively, the structure adjusts itself to peak near the maximum of $\nabla\beta_f$. Similar trends in mode structure are observed for calculations with $n = 2$, 4, and 6.

Figure 13 summarizes the calculated growth rates for both codes. The modes are strongly unstable, with $\gamma/\omega \lesssim 5\%$. GYRO finds that the growth rates of the core modes depend sensitively on the classical profile (figure 13(*a*)), the modes near q_{min} show some sensitivity (figure 13(*b*)), and the exterior modes are insensitive to the profile variations (figure 13(*c*)). TAEFL finds that the growth rate is about half as large for off-axis injection as for on-axis injection (figure 13(*d*)).

It is not possible to compare these calculations directly with experiment for many reasons. First, in experiment, instabilities are observed after the modes have grown to detectable levels, so measurements of linear growth rates are unavailable. Second, as shown in figure 10, owing to fast-ion transport, the actual variations in fast-ion profile are considerably smaller than the classically expected profiles used in the gyrofluid and gyrokinetic calculations. Third, the experimental modes change rapidly in time and the time-averaged mode amplitudes of figure 8 do not necessarily correspond to the modes calculated by TAEFL and GYRO at a particular instant. Fourth, the measured quantity is $\delta T_e/T_e$, which is not identical to γ. Despite these many caveats, some correspondence between observed mode amplitudes and linear stability trends is expected. The suppression of core TAEs by off-axis injection is correctly predicted by GYRO (figure 13(*a*)). The qualitative trend that modes in the core region are most sensitive to beam-injection angle (figure 13(*a*)), modes near q_{min} are moderately sensitive (figure 13(*b*)), and modes outside q_{min} are least sensitive (figure 13(*c*)) is another point of qualitative agreement. Robust instability of global TAEs is also consistent with experiment. However, the GYRO dependence of γ on beam profile is too weak for global TAEs (figure 13(*c*)) and TAEFL predicts a fairly weak dependence for the most unstable mode (figure 13(*d*)), while the experimental summed mode amplitude depends strongly on beam profile in all regions of

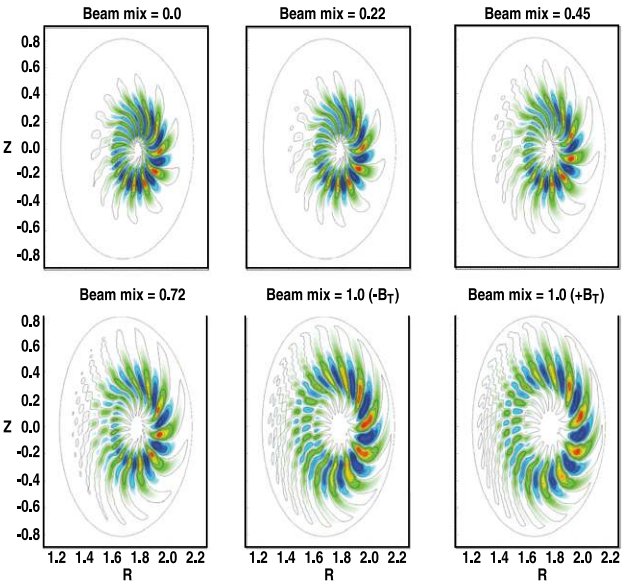

Figure 12. Linear eigenmode structure of the most unstable $n = 3$ mode for the six cases in the beam-mix scan as calculated by TAEFL.

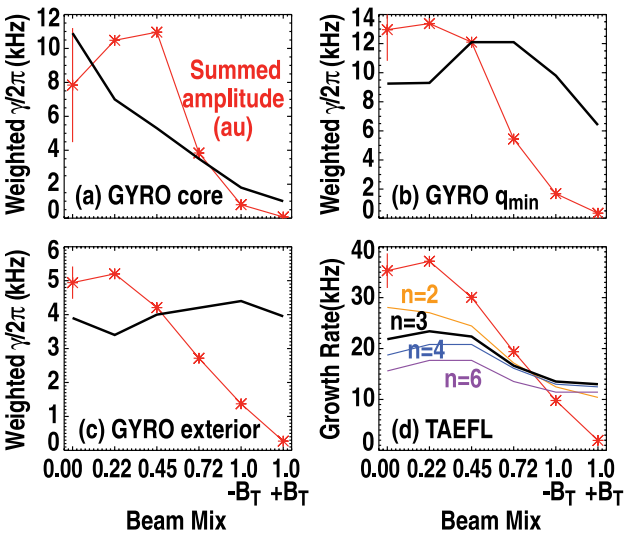

Figure 13. (*a*)–(*c*) GYRO calculations of the total growth rate of unstable $n = 3$ modes for the six cases in the beam-mix scan. The unstable modes are sorted by the spatial localization of their eigenfunctions into (*a*) core, (*b*) near $q_{\min}$, and (*c*) outside $q_{\min}$ modes. For global modes that overlap spatial regions, the contribution is weighted by the fraction of the eigenfunction in that region. (*d*) TAEFL calculations of the growth rate of the most unstable mode for four values of toroidal mode number n for the six cases in the beam-mix scan. For comparison, the experimentally measured summed mode amplitudes of figure 8 from (*a*) inside $q_{\min}$, (*b*) near $q_{\min}$, and (*c*), (*d*) outside $q_{\min}$ are also shown (*).

the plasma. During on-axis injection in the experiment, fast-ion transport by core modes may steepen $\nabla\beta_f$ outside $q_{\min}$, resulting in a larger average mode amplitude in the outer region.

4.2. Critical-gradient model

A 1.5D quasilinear model was recently published [26] that is designed to describe cases where the energetic particle drive

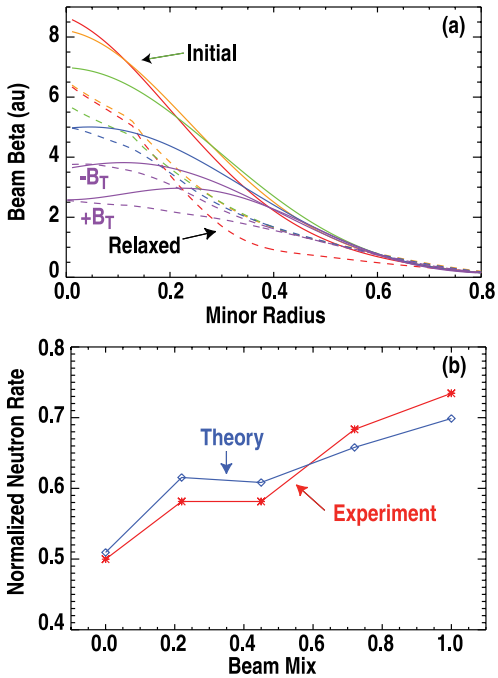

Figure 14. (*a*) Initial (solid) and redistributed (dashed) fast-ion profiles for the six cases in the beam-mix scan of figure 8(*a*) as calculated by the NOVA-based critical-gradient model. The plotted profiles are the average of profiles calculated at 465 and 565 ms. (*b*) Measured (*) and predicted (◇) neutron rate for the five discharges with negative B_T in the beam-mix scan. The measurements are time-averages between 420–600 ms that are normalized by the classically expected rate (using the corrected beam power). The theoretical points are time-averages between 365 and 565 ms and are divided by a factor of 1.32 to facilitate comparison.

substantially exceeds the stability limit. If the calculated fast-ion gradient exceeds marginal stability, the model diffuses particles in phase space until the fast-ion gradient reaches a critical value and the modes stabilize. The stability threshold is computed using local theories and ideal MHD simulations of TAE damping and growth rates. Application of the model to a DIII-D case similar to the ones studied here gave semi-quantitative agreement with measured neutron rates.

This model is applied to the six cases in the beam-mix scan. As in section 4.1, the plasma profiles are held fixed for all six cases and the initial fast-ion profile is the classically predicted one (figure 8(*a*)). Figure 14(*a*) shows the predicted relaxation of the profiles. (There is considerable variation in the predicted profiles at different times in the discharge; the figure shows time-averaged profiles.) Qualitatively, with one exception, the profiles are similar in all cases, as observed experimentally (figure 10). This is the expected result for a condition with many strong resonances [24] that is strongly driven past marginal stability. The calculated diffusion rate in a similar plasma is 7 m^2 s^{-1} [24], so it is plausible that the profiles relax in $\lesssim$10 ms, a time short compared with the $O(100\,\text{ms})$ slowing-down time.

Figure 14(*b*) compares the measured neutron rate with the predictions of the critical-gradient model. Somewhat fortuitously, the agreement is excellent. (Poorer agreement is observed for different time-averages of the theoretical prediction; also, the experimental normalization to the

classically expected rate is uncertain due to uncertainties in beam power and neutron calibration.) Although this excellent agreement should *not* be viewed as *quantitative* confirmation of the 1.5D model, it does suggest that the fundamental assumptions of a critical-gradient model are operative in these plasmas.

5. Conclusion

As theoretically expected, reducing $\nabla\beta_f$ is stabilizing for RSAEs and TAEs. In the present regime with numerous resonances with small amplitude modes, a critical-gradient model provides a reasonable description of profile flattening.

Experimentally, in future work, more accurate measurements of the time evolution of the fast-ion gradient are desirable. Theoretically, a grand challenge is to predict the nonlinear evolution of the modes and fast ions self-consistently in conditions like these. Alternatively, a critical-gradient model could be employed once the elements of the linear stability calculations have been quantitatively validated.

Acknowledgments

We thank the DIII-D team for their support. This work was funded by the US Department of Energy under SC-G903402, DE-FC02-04ER54698, DE-AC02-09CH11466 and DE-AC05-0000R22725.

References

[1] Cheng C.Z., Chen L. and Chance M. 1985 *Ann. Phys.* **161** 21
[2] Wong K.L. *et al* 1991 *Phys. Rev. Lett.* **66** 1874
[3] Heidbrink W.W., Strait E.J., Doyle E., Sager G. and Snider R.T. 1991 *Nucl. Fusion* **31** 1635
[4] Kusama Y. *et al* 1998 *Nucl. Fusion* **38** 1215
[5] Sharapov S.E. *et al* 2001 *Phys. Lett.* A **289** 127
[6] Breizman B.N., Berk H.L., Pekker M.S., Pinches S.D. and Sharapov S.E. 2003 *Phys. Plasmas* **10** 3649
[7] Fasoli A. *et al* 2007 *Nucl. Fusion* **47** S264
[8] Fu G.Y. and Van Dam J.W. 1989 *Phys. Fluids* B **1** 1949
[9] Fasoli A. *et al* 2010 *Plasma Phys. Control. Fusion* **52** 075015
[10] Strait E.J., Heidbrink W.W., Turnbull A.D., Chu M.S. and Duong H.H. 1993 *Nucl. Fusion* **33** 1849
[11] Murphy C.J. *et al* 2011 Overview of DIII-D off-axis neutral beam project *SOFE: Proc. 24th Symp. on Fusion Engineering (Chicago)*
[12] Heidbrink W.W. *et al* 2012 *Nucl. Fusion* **52** 094005
[13] Van Zeeland M.A. *et al* 2006 *Phys. Rev. Lett.* **97** 135001
[14] Van Zeeland M.A. *et al* 2007 *Phys. Plasmas* **14** 056102
[15] Van Zeeland M.A. *et al* 2009 *Nucl. Fusion* **49** 065003
[16] Tobias B. *et al* 2011 *Phys. Rev. Lett.* **106** 075003
[17] Tobias B.J. *et al* 2011 *Phys. Plasmas* **18** 056107
[18] Spong D.A. *et al* 2012 *Phys. Plasmas* **19** 082511
[19] Chen Y. *et al* 2013 *Phys. Plasmas* **20** 012109
[20] Heidbrink W.W. *et al* 2007 *Phys. Rev. Lett.* **99** 245002
[21] Heidbrink W.W. *et al* 2008 *Nucl. Fusion* **48** 084001
[22] Pace D.C., Fisher R.K., García-Muñoz M, Heidbrink W.W. and Van Zeeland M.A. 2011 *Plasma Phys. Control. Fusion* **53** 062001
[23] Van Zeeland M.A. *et al* 2011 *Phys. Plasmas* **18** 056114
[24] White R.B., Gorelenkov N, Heidbrink W.W. and Van Zeeland M.A. 2010 *Plasma Phys. Control. Fusion* **52** 045012
[25] White R.B., Gorelenkov N., Heidbrink W.W. and Van Zeeland M.A. 2010 *Phys. Plasmas* **17** 056107
[26] Ghantous K., Gorelenkov N.N., Berk H.L., Heidbrink W.W. and Van Zeeland M.A. 2012 *Phys. Plasmas* **19** 092511
[27] Rice B.W., Nilson D.G. and Wroblewski D. 1995 *Rev. Sci. Instrum.* **66** 373
[28] Gohil P., Burrell K.H., Groebner R.J. and Seraydarian R.P. 1990 *Rev. Sci. Instrum.* **61** 2949
[29] Luo Y., Heidbrink W.W., Burrell K.H., Gohil P. and Kaplan D. 2007 *Rev. Sci. Instrum.* **78** 033505
[30] Muscatello C.M., Heidbrink W.W., Taussig D. and Burrell K.H. 2010 *Rev. Sci. Instrum.* **81** 10D316
[31] Grierson B.A. *et al* 2012 *Rev. Sci. Instrum.* **83** 10D529
[32] Pankin A., Mccune D., Andre R., Bateman G. and Kritz A. 2004 *Comput. Phys. Commun.* **159** 157
[33] Murakami M. *et al* 2009 *Nucl. Fusion* **49** 065031
[34] Fu G.Y. 1995 *Phys. Plasmas* **2** 1029
[35] Austin M.E. and Lohr J. 2003 *Rev. Sci. Instrum.* **74** 1457
[36] Tobias B. *et al* 2010 *Rev. Sci. Instrum.* **81** 10D928
[37] Van Zeeland M.A. *et al* 2005 *Plasma Phys. Control. Fusion* **47** L31
[38] Gupta D.K., Fonck R.J., Mckee G.R., Schlossberg D.J. and Shafer M.W. 2004 *Rev. Sci. Instrum.* **75** 3493
[39] Bass E.M. and Waltz R.E. 2010 *Phys. Plasmas* **17** 112319